



Commissioning of the ELENA B-train system

Author(s): Anthony Beaumont, Marco Buzio, David Giloteaux, Christian Grech, Marco Roda, Nicholas Sammut (University of Malta)

TE Department

Keywords: B-train, ELENA, induction coil, NMR, FESA, magnetic measurements

Distribution:

TE-MS-MM



Commissioning of the ELENA B-train system

Abstract

This note contains information on the installation and commissioning of the B-train system at the Extra Low Energy Antiproton (ELENA) ring. In particular, the characterization of the sensors and analysis made on series magnet measurements will be described, as well as a new measurement model which was constructed to optimally link theoretical concepts to empirical observations. An uncertainty quantification of the measurement system follows as well as a performance overview and validation of the system with the beam.

PREPARED BY:	CHECKED BY:	APPROVED BY:
Anthony Beaumont, Marco Buzio, David Giloteaux, <u>Christian Grech</u> , Marco Roda TE-MSC-MM Nicholas Sammut University of Malta	S. Russenschuck TE-MSC-MM	S. Russenschuck TE-MSC-MM

DISTRIBUTION LIST:
TE-MSC-MM



HISTORY OF CHANGES

REV. NO.	DATE	PAGES	DESCRIPTION OF THE CHANGES
0.0	May 14, 2019	All	Document created



TABLE OF CONTENTS

Abstract	2
History of Changes	3
Contents	4
Definitions	6
1 Introduction	8
1.1 Extra Low Energy Antiproton ring	8
1.2 B-train systems in synchrotrons	9
1.2.1 Induction coil measurements	10
1.2.2 Field marker sensors	10
1.2.3 B-train measurement model	12
1.3 FIRESTORM project	12
1.4 ELENA B-train commissioning specifications	13
2 Measurement model	16
2.1 Introduction	16
2.2 Measurement model	16
2.2.1 Objective	16
2.2.2 Field integral measurement	17
2.2.3 Flux integration	17
2.2.4 Integration constant	18
2.2.5 Model definition	18
2.3 Parameter identification	19
2.3.1 Effective coil width, \bar{w}_{eff}	19
2.3.2 Integration constant, \mathbb{I}_0	20
2.3.3 Induction coil gain error, η	20
2.3.4 Reference-to-ring error, α	22
2.3.5 Coil offset factor, ε	23
2.3.6 Mapping the model to FPGA registers	24
3 Uncertainty quantification	26
3.2 Introduction	26
3.3 Uncertainty quantification background	26
3.3.1 Determining the combined standard uncertainty	27
3.4 Combined uncertainty of the ELENA B-train system	27
3.5 Conclusion	29



4	Metrological Characterization and Verification	30
4.1	Introduction	30
4.2	Characterizing ELENA B-train performance	30
4.2.1	Error characterization model	30
4.2.2	Definitions	30
4.2.3	Results	32
4.3	Metrological verification with beam	32
4.3.1	Experimental results	34
	Conclusions	37
	References	37
	Acknowledgements	38
	Appendix	39
	References	39



Definitions

B	magnetic field
B_0	central magnetic field
B_{NMR}	NMR corresponding magnetic field
\dot{B}	rate of magnetic field wrt time
$\int Bdl$	integral magnetic field
$\int Bdl_{nom}$	nominal integral magnetic field
$\int Bdl_{ref}$	reference magnet's integral magnetic field
$\int Bdl_{ring}$	synchrotron's integral magnetic field
c	speed of light in vacuum
f_{rev}	revolution frequency
$\int Gdl$	integrated field gradient
I	magnetization current
k_{integ}	integrator gain
l	length
l_m	effective magnetic length
l^*	nominal magnetic length
m_0	particle rest mass
n	field marker number
N	number of turns
q	particle charge
R	radius
R_{coil}	coil resistance
$R_{B-train}$	B-train input resistance
s	transversal beam path
S	surface
t	time
TF	transfer function
V_c	induced voltage



δV_0	drift voltage
ΔV	voltage amplitude
w_{avg}	average width
w_{eff}	effective width
α	integral field ratio
γ	gyromagnetic ratio
ε	coil offset factor
η	coil correction factor
θ	beam deflection
ρ	synchrotron bending radius
ρ_r	resistivity
σ	standard deviation
Φ	magnetic flux
Φ_0	residual magnetic flux
$\Delta\Phi$	the magnetic flux change

1 Introduction

1.1 Extra Low Energy Antiproton ring

The Extra Low Energy Antiproton ring (ELENA) is a CERN project aiming to construct a small 30.4 m circumference synchrotron to further decelerate antiprotons from the Antiproton Decelerator (AD) from 5.3 MeV down to 100 keV. Decreasing the energies to this level, and the use of an electron cooler to reduce emittance will allow the six different antimatter experiments to increase their antiproton capture efficiency and creates the possibility of rendering new kinds of experiments.

Commissioning of the ELENA ring started in November 2016 and culminated in August 2017 with the first antiproton beam circulating in the ring. The beam of antiprotons was successfully injected and it was observed circulating for a few thousand turns. Fig. 1.1 shows the mechanically finished ring with nearly all its main components at the start of first beam. As antiprotons are difficult to produce and they need to be shared among six experiments, progress in the commissioning of ELENA was also made using protons and ions coming from a local H^- ion and proton source. In this way, the commissioning phase sped up and by the end of 2018, ELENA will be ready to provide first antiproton beams for tests to the Gbar experiment, which will investigate the behaviour of antihydrogen under the effect of gravity.

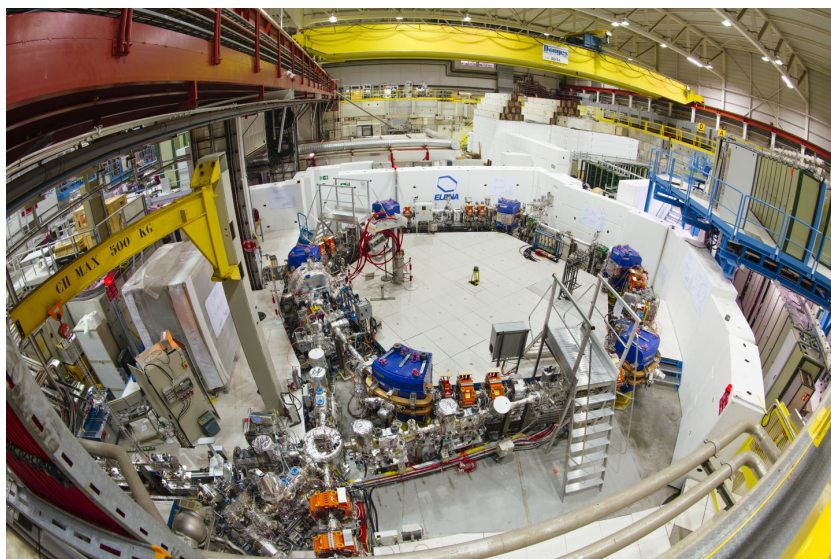


Fig. 1.1: The ELENA ring at the start of first beam [1]

1.2 B-train systems in synchrotrons

The operation of synchrotrons is based on Radio Frequency (RF) cavities, which control the speed of the particles by inducing an electric field such that particles move in one direction only. The other important components in a synchrotron are the dipole bending magnets, which make sure that the beam of particles goes round in a circular trajectory. Hence, the knowledge of $\bar{B}(t)$, the average magnetic field over the number of dipole magnets making up the synchrotron in real-time is essential for beam control. There are two different ways to determine the magnetic field in ramped machines. One approach is the use of a software magnetic model to calculate and predict the magnetic field via the regulation of the power converter. The other method is based on a signal originating from several sensors situated in a reference magnet. Both methods have their own advantages and disadvantages, but practical experience over recent years has shown that the use of sensors can lead to significant improvements [2]. Hence a real-time measurement system called the B-train is used to transmit $\bar{B}(t)$ to users, mainly operators of the RF cavity. At CERN, $\bar{B}(t)$ is distributed using the B-train system in the Low Energy Ion Ring (LEIR), the Proton Synchrotron Booster (PSB), the Proton Synchrotron (PS), the Super Proton Synchrotron (SPS), the AD and the ELENA ring. Using the B-train's transmitted $\bar{B}(t)$ value, $f_{rev}(t)$ is determined using the Equation 4.6 below and changes according to $\bar{B}(t)$.

$$f_{rev}(t) = \frac{c}{2\pi} \cdot \sqrt{1 - \frac{1}{1 + \left(\frac{\bar{B}(t)\rho q}{m_0 c}\right)^2}} \quad (1.1)$$

where c is the speed of light in vacuum, q is the particle charge, m_0 is the particle rest mass and ρ is the machine's bending radius.

A typical B-train system configuration is shown in Fig. 1.2. Each system includes two types of sensors installed within the reference magnet: induction coils which span the central path of the magnet as well as a local sensor, termed field marker, which is placed in the centre of the magnet.

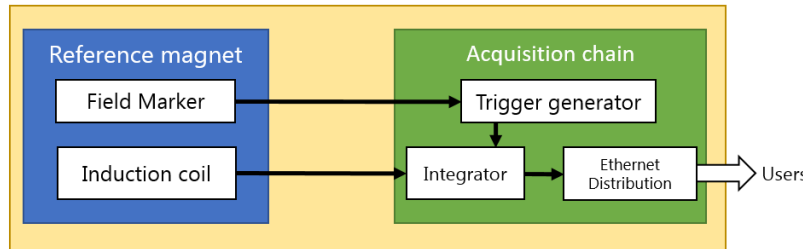


Fig. 1.2: Block diagram of measurement system

1.2.1 Induction coil measurements

A fluxmeter is an instrument consisting of several induction coils wound in a loop, which is typically used for measuring the magnetic flux. The fluxmeter principle is based on the magnetic induction law [3], where each coil with surface S , is exposed to a magnetic field B , resulting in magnetic flux Φ , linked with the coil:

$$\Phi = \int_S B dS \quad (1.2)$$

A variation in time of the flux linked by the coil induces a coil voltage V_c , proportional to the rate of change, or:

$$V_c = - \frac{d\Phi}{dt} \quad (1.3)$$

As shown in Equations 1.2 and 1.3 a voltage can be induced in the coil either by varying the magnetic field, or by changing the orientation of the coil (dS/dt). In the case of a magnetic field variation in time the coil is usually kept static, and the fluxmeter provides a measurement of the flux change between two time markers. In the case of static magnetic fields, the coil is moved; a technique which requires precision. In real-time measurements of synchrotrons, dynamic magnetic fields are measured, and hence a static induction coil is employed.

One of the benefits of this instrument is that an induction coil is a linear device and its sensitivity can be designed according the field to be measured. This makes the fluxmeter a viable option for a vast range of field measurement. In practice the application of the induction method is restricted to field levels above $0.1 \mu\text{T}$, with no specific limitation at the upper end. Another strong point in favour of fluxmeters is the flexibility in the design of the instrument. In the case of the ELENA ring, since the dipole magnets are curved, beam dynamics require the field integral to be measured along the path followed by the particles. Hence the fluxmeter is designed such that the coils are curved in the same shape as the poles of the magnet.

The main limitation in fixed coil measurements is the small voltage offset generated by parasitic currents in the electronics or thermal voltages. An input voltage offset results in a visible field drift that often cannot be distinguished from the physical field change [3]. When the measurement is longer than a few seconds, then this phenomenon becomes significant, and hence the voltage offset must be removed before the integration occurs.

1.2.2 Field marker sensors

A field marker is a magnetic field sensor, which triggers a digital signal at $t = t_k$ when $B = B_0$. As a result, it provides an accurate absolute field value at one point in time. Nuclear Magnetic Resonance (NMR) is the leader in field marker sensors, providing the best accuracy for a wide magnetic field range [4]. The operating principle of NMR is based on the precession frequency of the proton spin in the nucleus, which varies linearly with the magnetic field amplitude, by means of a gyromagnetic ratio ($\gamma = 42.57608 \text{ MHz/T}$). The commercial NMR equipment is designed to operate in teslameter

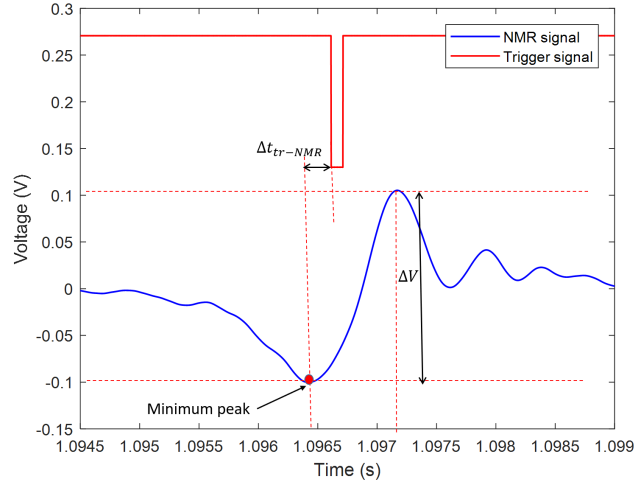


Fig. 1.3: NMR signal and resulting trigger signal

mode, by sweeping the frequency and locking on the occurrence of the resonance curve. The innovative instrumentation aspect of the field marker measurement in synchrotrons is the use of a commercial teslameter in marker mode in a changing field, where the NMR probe is excited at a given frequency by a RF generator. The NMR signal in Fig. 1.3 is generated according to the resonant frequency set and is characterised by the voltage amplitude ΔV . A peak detector subsequently detects the minimum peak of the signal and generates a trigger signal with a delay of Δt_{tr-NMR} .

Since NMR requires a homogeneous field for correct operation, one may consider the use of Ferri-magnetic Resonance (FMR) markers, which make use of the electron spin resonance phenomenon, based on the difference between the energy emitted and absorbed by electrons switching between opposite spin states. Due to small probe sizes and comparatively low Q-values, considerable field gradients can be tolerated [5]. In addition, FMR markers are compatible with commercially available NMR teslameters and hence FMR probes can be interchanged with NMR probes quite easily. On the other hand, FMR is limited to fields larger than 60 mT, the excitation signal has a broad resonance peak (making it more difficult to detect the peak), and it is temperature-dependant as it has to be optimized for each specific application.

In a metrological characterization of the NMR marker reported in [6], the most critical conditions were found at low field. At field levels lower than 47 mT, a reproducibility better than $4.5 \mu\text{T}$ was found using slow ramp rates ($B/\dot{B} > 0.8 \text{ s}$), while for faster ramp rates, it was better than $9 \mu\text{T}$. For a high-field marker using a high ramp rate, the reproducibility was found to be better than $3 \mu\text{T}$. In another comparative study between the FMR and NMR sensors [7], NMR sensor results was found to be slightly more repeatable across all target field levels and ramp rates and it was chosen as the

best candidate for the operation of the ELENA ring.

1.2.3 B-train measurement model

For the measurement of the magnetic field in real-time, a combination of induction coils and field markers is used. The B-train is designed to output the average field $\bar{B}(t)$ over each of the bending dipoles in the ring. It is based on the combination of the induced voltage in the coil, V_c , and B_m , the field marked at time t_k , where $k = 1, 2, \dots, n$ for multiple field markers:

$$\bar{B}(t) = B_m(t_k) + \frac{1}{A_c} \int_{t_k}^t V_c(\tau) d\tau \quad (1.4)$$

where A_c is the effective area of the induction coil. For the ELENA B-train, a more comprehensive measurement model will be implemented, which incorporates theoretical concepts with empirical observations from each individual magnet. The ELENA B-train is a good trial machine for this attempt, due to the fact that it is still in its commissioning stages, all the magnets were measured separately, and so data from each individual magnet is already available.

1.3 FIRESTORM project

The B-train instrument has been used at CERN for decades in the LHC injector chain and Antimatter Factory. Since the instruments started operating, most of the measurement technology became obsolete, and critical electronic components which are unique and unrepairable started ageing. Besides this, due to the upgrade of synchrotrons along the years, the requirements for the B-train became more and more stringent. Another issue was that the instrument's composition was not uniform across accelerators, causing the management of these instruments to be more difficult.

The Field In REal-time STreaming from Online Reference Magnets (FIRESTORM) project is being carried out with the aim of upgrading all B-train systems at CERN. The modernised B-train system addresses the shortcomings of the current B-train systems and consolidates the existing B-train systems under common hardware/software platforms. The project emphasises a uniform system across the whole CERN complex, which uses modern digital off-the-shelf technology and/or CERN-developed components. Another feature is that in cases where there is an existing B-train system, it allows operation in parallel with old systems.

The electronic system accompanying the sensor setup can be seen in Fig. 1.4. The whole setup consists of two chains; C1 and C2, where C1 is the operational chain and C2 is the spare chain. Both chains consist of a B-train Integral FMC (FPGA Mezzanine Card), which integrates the coil voltage, field marker cards, which detect the peak of the field marker resonance signal and send a trigger signal, as well as a Predicted B FMC which transmits the value of the magnetic field based on a simulation. Additionally, new B-train systems make use of the CERN-developed White Rabbit

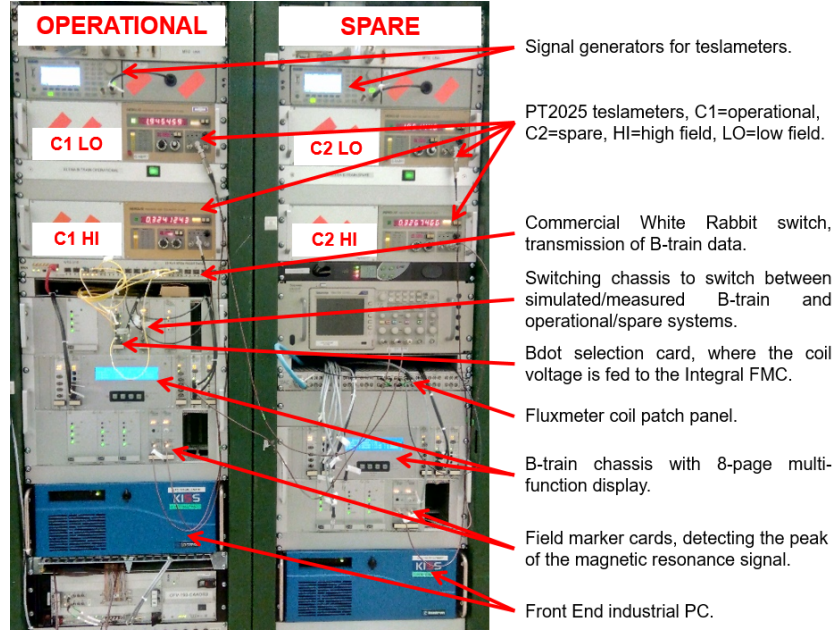


Fig. 1.4: ELENA FIRESTORM electronics

network to transmit $barB(t)$ values. The system distributes digitally absolute values of $barB$ and its derivative in Ethernet frames at 250 kHz.

Due to the large number of devices at CERN, the implementation of front end devices into the CERN control system is not an easy task. Hence, a framework was developed called FESA (Front End Software Architecture) and its goal is to use an executable program (device class), which runs on the user's front-end CPUs and which performs all of the required tasks, such as getting and setting data [8]. The framework does not include a final graphical user interface, but a flexible test environment to check all functions of the class. As part of the B-train system, the FESA interface is used to set and get data from registers in the FPGA, which are used to calculate the magnetic field using the various sensors.

1.4 ELENA B-train commissioning specifications

The ELENA ring's aim is to decelerate anti-protons delivered by the AD, from 5.3 MeV down to 100 keV and to increase the number of trapped anti-protons. The ELENA ring will hence be operated at an unusually low energy for a synchrotron with a magnetic focusing structure [9]. Fig. 1.5 shows the cycles employed to power the magnets in the ELENA ring. In the decelerating cycle, magnets are first ramped up to a momentum level of 100 MeV/c to match the energy of the beam incoming from the AD, and then the beam is slowed, first to a level of 35 MeV/c and then to

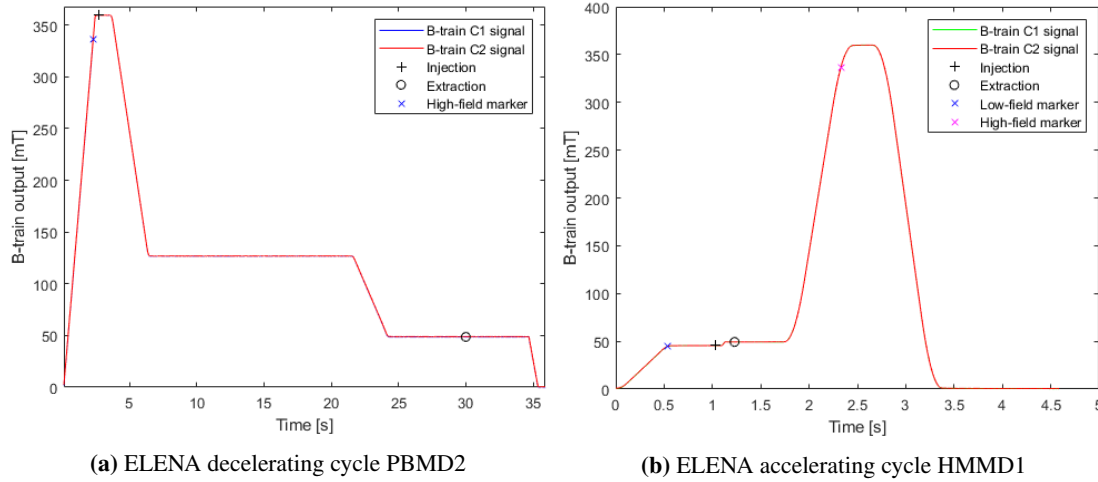


Fig. 1.5: Main cycles used in the ELENA ring

13.7 MeV/c using an electron cooling process. In the accelerating cycle, H^- particles are injected at 13.7 MeV/c.

Obtaining a good magnetic field quality is challenging, due to the very low magnetic fields required and remanence and hysteresis effects. One of the biggest challenges in real-time magnetic measurement is the extremely low ejection field of 50 mT, where the beam line is vulnerable to external field perturbation due to electric lines and other elements. In general, the emphasis is placed upon the reproducibility of the measured field rather than on its absolute accuracy. Reproducibility is, as a rule, adversely affected by operation at low field due to remanent field effects, which exacerbates the effects of hysteresis [10]. The complete specifications for the ELENA B-train are listed in Table 1.1.

The novel approach which will be taken for the commissioning of the ELENA B-train includes the addition of the second field marker, in order to provide a better measurement at both low and high field levels, the implementation of an improved measurement model, as well as adapting the B-train software for bipolar measurement and transmission of the magnetic field. The full sensor setup used for the ELENA B-train can be seen in Fig. 1.6.

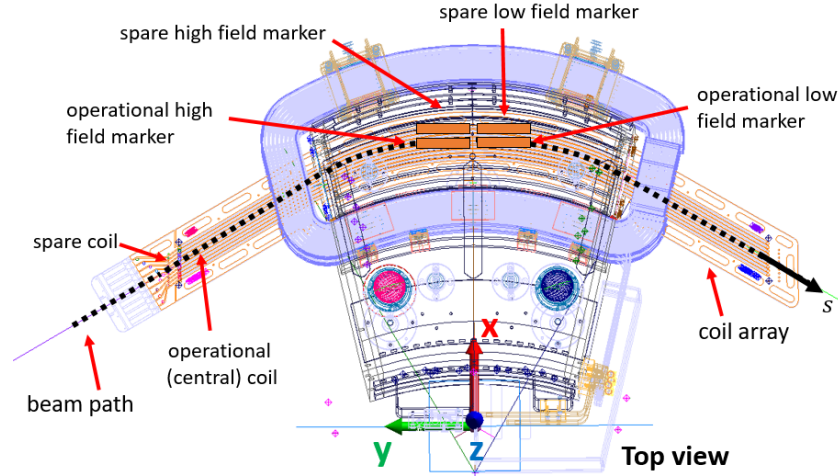


Fig. 1.6: Sensor setup for ELENA B-train

Table 1.1: Cycle Properties and timings for separate chains C1 and C2

Parameter	Symbol	Unit	Deceleration		Acceleration	
			C1	C2	C1	C2
Injection time	t_{inj}	ms	2727		1029	
Extraction time	t_{ex}	ms	30000		1229	
B-train output at t_{inj}	$\bar{B}(t_{inj})$	G	3593		454.6	
B-train output at t_{ex}	$\bar{B}(t_{ex})$	G	493		492.7	
Current at t_{inj}	$I(t_{inj})$	A	276		34.8	
Current at t_{ex}	$I(t_{ex})$	A	38		37.8	
Field marker trigger time	t_k	ms	2315.0	2314.4	535.2/2328	535.0/232.7
Field marker value	$\bar{B}(t_k)$	G	3400		450/3400	450/3400
Ramp rate at t_k	$\dot{B}(t_k)$	G/s	1600		1000/6500	1000/6500
Average current drift	$\langle \dot{I} \rangle$	A/s			0.00054	
Current repeatability	$\sigma(I)$	A			0.0028	
Nominal current-to-field ratio	\bar{B}/I	G/A			13.01	

2 Measurement model

2.1 Introduction

In this chapter, we present a measurement model for estimating the magnetic field of a synchrotron-type particle accelerator, based on sensors installed in a reference magnet. The model combines the calibration of the individual sensors with the experimental characterization of the magnets to infer, in absolute terms, the value of the average field in the ring, as needed for the real-time feedback control of the ELENA ring.

As discussed in the previous chapter, a B-train system consists of a static induction coil and a field marker sensor. While individual calibration of these sensors is relatively straightforward, characterization of the system as a whole presents several difficulties. First, the coil can be offset from the desired central position in the magnet gap, due to alignment tolerances or space constraints. Secondly, the marker is usually a millimeter-size sensor, such as a Hall plate or a magnetic resonance probe, from which we must somehow infer an average over a path up to several meters long. Finally, unavoidable material and geometric uncertainties inherent in the fabrication process may lead to a difference between the field in the instrumented magnet and the average field seen by the particles in the ring. These error sources are usually compensated by means of an overall *ad-hoc* factor, ensuring as much as possible the experimental match between field, particle bending radius and momentum, consistent with the well-known Larmor's expression[11]. Such a shortcut, however, is not fully satisfactory: in the context of an accelerator chain, absolute knowledge of the field would be far preferable to ensure energy matching and seamless beam transfer between rings. Absolute calibration of our instrument is however not possible, since a suitable reference standard for the field along a path up to several hundred meters long is not available. The aim of this work is rather to build an explicit measurement model, to infer indirectly the average field in the accelerator ring from the output of sensors placed elsewhere.

2.2 Measurement model

2.2.1 Objective

The B-train is designed to output the average field \bar{B} over each of the bending dipoles, assumed to be identical to each other:

$$\bar{B}(t) = \frac{\mathbb{I}(t)}{l^*} \quad (2.1)$$

where:

$$\mathbb{I}(t) = \int_{-\infty}^{\infty} B(t, s) ds \quad (2.2)$$

is the integral magnetic field produced by each magnet, $B(t, s)$ is the field profile inside each magnet as a function of time and of the longitudinal co-ordinate, s (see Fig. 1.6), and:

$$l^* = \frac{2\pi\rho}{N_B} \quad (2.3)$$

is the fraction of the circumference associated to each dipole, where $\rho = 0.927$ m is the nominal bending radius of the ring [12] and $N_B = 6$ is the number of bending dipole magnets. The integration limits in (2.2) are extended for simplicity to infinity. This is warranted whenever, as in our case, the length of the coil allows to capture the whole magnetic field produced within the requested tolerance, and at the same time there is no interference between adjacent magnets. In the following, we shall use interchangeably the time t and the excitation current $I = I(t)$ as independent variables, assuming that only one cyclic waveform is used and that the inverse relationship $t(I)$ be uniquely defined on either branch of the hysteresis loop.

2.2.2 Field integral measurement

The integral field, $\mathbb{I}(t)$, is derived from the magnetic flux linked through the coil. At any given time, taking into account that the variation of the field in the direction transverse to each coil is negligible, we can express the flux as:

$$\Phi(t) = N_T \int_{-\infty}^{\infty} w(s)B(t, s)ds = w_{\text{eff}}(t) \int_{-\infty}^{\infty} B(t, s)ds \quad (2.4)$$

where N_T is the number of winding turns, $w(s)$ is the winding width (variable along the coil due to manufacturing tolerances) and w_{eff} is the effective width, defined by:

$$w_{\text{eff}}(t) = \frac{\Phi(t)}{\mathbb{I}(t)} = \frac{N_T \int_{-\infty}^{\infty} w(s)B(t, s)ds}{\int_{-\infty}^{\infty} B(t, s)ds} \quad (2.5)$$

The effective width represents the average geometric coil width, weighted by the field profile and thus depending upon the magnet being tested. In general, as the field level increases, the iron yoke may get into saturation, increasing flux leakage and flattening the field profile, thus potentially affecting w_{eff} . In our case saturation is negligible, so we can use an average effective width, that is practically a constant and may be defined as:

$$\bar{w}_{\text{eff}} = \frac{\Phi(\bar{t})}{\mathbb{I}(\bar{t})} \quad (2.6)$$

where \bar{t} is the time at which the nominal excitation current of the dipoles $\bar{I} = I(\bar{t})$ is attained.

2.2.3 Flux integration

The flux through the coil is derived by combining the output of the two sensors in the following manner. The time axis is split into a succession of integration intervals $t_k \leq t < t_k + 1$, with $k =$

1, 2, ... where each t_k represents the time at which a field marker trigger is received. During each interval, ideally:

$$\mathbb{I}(t) = \mathbb{I}(t_k) + \Delta\mathbb{I} = \mathbb{I}_0 + \frac{\Delta\Phi(t)}{\bar{w}_{\text{eff}}} \quad (2.7)$$

where, without loss of generality, \mathbb{I}_0 represents the integration constant at the field marker level being considered and, according to Faraday's law [3]:

$$\Delta\Phi(t) = - \int_{t_k}^t (V_c(\tau) - \delta V) d\tau \quad (2.8)$$

In (2.8), δV refers to the unavoidable voltage offset caused by parasitic currents in the electronics and thermoelectric effects. In our system, this can be high as $60 \mu\text{V}$ leading to a field drift of the order of $10 \mu\text{T/s}$. As the offset is observed to fluctuate randomly over time scales of seconds and longer, an effective systematic correction is not possible. Several strategies to estimate and correct it dynamically, are reviewed in [13]. The method adopted in all real-time CERN systems is to reset the integral at every t_k ; at least one, or optionally more, marker triggers per cycle can be generated, at low and/or high field, the choice depending upon the characteristics of the magnetic cycle being run. Upon reception of a trigger the output field value is artificially smoothed over a duration of 20 ms, in order to avoid discontinuities that could destabilize the beam. In this way, the field marker accomplishes the double task of providing both the coil integration constant and drift correction, and integration can proceed uninterrupted for up to several months.

2.2.4 Integration constant

The integration constant $\mathbb{I}(t_k)$ cannot be measured directly, since the field marker provides only a local value $B(t_k, 0)$ (albeit highly accurate and reproducible). In the past, the constant was obtained by multiplying the local field by a quantity called magnetic length, typically expressed as a function of the excitation current:

$$l_m(t(I)) = \frac{\mathbb{I}(t(I))}{B(t(I), 0)} \quad (2.9)$$

such that $\mathbb{I}(t_k) = l_m(I(t_k))B(t_k, 0)$. A fixed value of l_m , corresponding initially to the field level of interest but adjusted by trial and error, is implemented in all of CERN legacy systems. A novel absolute calibration method that provides directly the value of $\mathbb{I}(t_k)$ is discussed in Section 2.3.2.

2.2.5 Model definition

We can finally formulate the measurement model, by combining (2.1) and (2.7), adding in three further factors to represent non-ideal effects:

$$\bar{B}(t) = \frac{(1 + \alpha)(1 + \varepsilon)}{l^*} \left[(1 + \eta) \frac{\Delta\Phi(t)}{\bar{w}_{\text{eff}}} + \mathbb{I}_0 \right] \quad (2.10)$$

The term in square brackets represents the field integral measured by the combination of induction coil and field marker, where the integrated flux is corrected by the coefficient $1+\eta$. This compensates for the total gain error in the coil acquisition chain, including the coil effective width, pre-amplifier, anti-aliasing filter and the ADC. The coefficient $1+\varepsilon$ accounts for the possible coil offset with respect to the beam path, which may cause a systematic error due to the non-uniformity of the field in the transverse direction. Finally, the coefficient $1+\alpha$ accounts for any difference between the reference magnet and the average of the ring. The terms η , ε and α are all non-dimensional, and much smaller than one.

2.3 Parameter identification

We shall now proceed to discuss in detail each term in the model and the respective identification procedure, based on the results of the acceptance test campaign of the bending magnets for ELENA and on analysis of the acquisition chain.

2.3.1 Effective coil width, \bar{w}_{eff}

The effective width defined in (2.5), cannot be measured geometrically to the required precision; however, it can be calibrated magnetically in two different ways:

- from (2.6), by comparing a flux change acquisition to an independent measurement of $\Delta\mathbb{I}(\vec{r})$, such as can be obtained, in a curved magnet, with a finely spaced Hall-probe map. This method is time-expensive and requires the Hall probe map to be cross-calibrated against a more precise absolute reference, such as NMR or stretched-wire measurements.
- a relative cross-calibration can be obtained by comparing the i -th coil in an array against a reference coil, placed on top of it symmetrically across the magnet mid-plane, so that it sees essentially the same field inside a dipole magnet gap. The ratio of the measured flux differences provides the effective width, according to [14]:

$$\bar{w}_{\text{eff}}^i = \bar{w}_{\text{eff}}^{\text{ref}} \frac{\Delta\Phi^i}{\Delta\Phi_{\text{ref}}} \quad (2.11)$$

This method is effective to calibrate a large number of coils, when the absolute calibration of the reference coil is known.

The latter calibration procedure was carried out for the coil used for the ELENA B-train, leading to an estimate of $\bar{w}_{\text{eff}} = 2.8415$ m for the central coil with an uncertainty of $80 \mu\text{m}$ (2.8×10^{-5}), and $\bar{w}_{\text{eff}} = 2.8601$ m for coil no.7 used as part of C2.

2.3.2 Integration constant, \mathbb{I}_0

The integration constant is derived with an identification procedure that benefits from the availability of a bi-polar power supply and allows *in-situ* absolute integral field measurements with an induction coil, which would normally only see field changes. As shown in Fig. 2.1, the magnets are first degaussed to attain a demagnetized reference state. The residual magnetization \mathbb{I}_{res} is measured with a Hall probe, cross-calibrated with a fluxgate magnetometer in the range below 1 mT, and is about 0.03 mTm (80 ppm of the nominal field). Then, the excitation current is cycled and the flux change measured by the coil is integrated according to:

$$\mathbb{I}(t) = \mathbb{I}_{\text{res}} + \frac{\Delta\Phi(t)}{w_{\text{eff}}} \quad (2.12)$$

After an initial transient lasting three cycles, the magnet settles on a stable hysteresis loop that makes the field integral reproducible from cycle to cycle within a level of 400 ppm. The assumption of loop closure, which has been validated by independent NMR measurements, allows a very effective integrator drift correction on the stable cycles. The integration constant is finally derived by averaging over $n \geq 7$ stable cycles:

$$\mathbb{I}_0 = \frac{1}{n} \sum_{j=3}^{3+n} \mathbb{I}(t_j) \quad (2.13)$$

This calibration procedure has been carried out repeatedly at two different field levels, and the uncertainty of the result has been estimated from standard deviation of the results:

- $\mathbb{I}_0 = 326.836 \text{ mTm @ } 340 \text{ mT}, u(\mathbb{I}_0) = 13 \text{ } \mu\text{Tm}$
- $\mathbb{I}_0 = 43.125 \text{ mTm @ } 45 \text{ mT}, u(\mathbb{I}_0) = 12 \text{ } \mu\text{Tm}$

The procedure should be repeated every time that the cycle waveform or the field marker level are changed; the impact of doing so on operation is minimal as the necessary time, including setup of the acquisition system, semi-automated post-processing and results upload, is only a few hours.

2.3.3 Induction coil gain error, η

The factor $1+\eta$ accounts for errors in the gain of the electronic coil acquisition chain, schematically represented in Fig. 2.2, where R_c and L_c are the inductance and resistance of the coil respectively, R_{in} is the input resistance of the integrator electronics and C represents the sum of distributed capacitance between the coil windings and the shielded cable. Two major error sources are considered: the loading effect due to the finite input resistance of the integrator compared to the coil resistance, and the internal error k_{int} of the input stage of the integrator (including an ADC and an anti-aliasing filter). We remark that the relevant frequency content of the magnetic field waveform

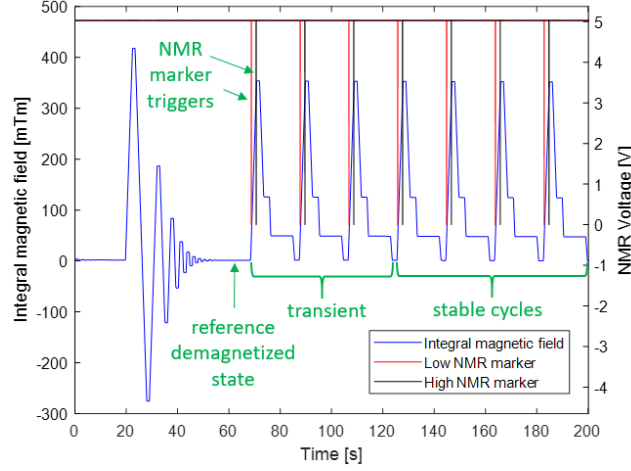


Fig. 2.1: Absolute *in-situ* calibration of field markers

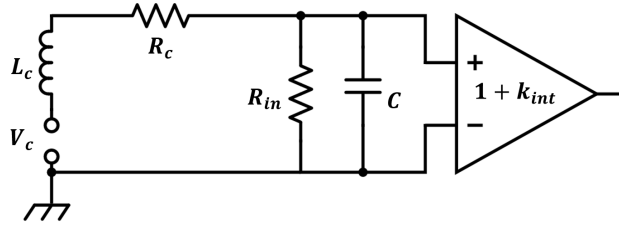


Fig. 2.2: Equivalent model of the acquisition chain

does not exceed typically 100 Hz, so that the low-frequency approximation applies. Combining these parameters, the loading effect is defined in (2.14) as:

$$1 + \eta = \left(1 + \frac{R_c}{R_{in}}\right) (1 + k_{int}) \quad (2.14)$$

The identification procedure for these parameters can be summarized as follows:

- The coil and input resistances can be easily obtained to the required accuracy using a multi-meter [15]. For the ELENA system, we find that $R_c \simeq 5 \text{ k}\Omega$ and $R_{in} \simeq 2 \text{ M}\Omega$. The nominal uncertainty of the resistance measurements in the range considered is 150 ppm, which is negligible compared to the standard deviation of ambient temperature, estimated around $0.7 \text{ }^\circ\text{C}$ over a year of machine operation. Taking into account the temperature coefficient of the resistivity of copper i.e. $0.004 \text{ }^\circ\text{C}^{-1}$, the relative uncertainty of R_c is the order of 0.3%.
- The integrator gain can be verified by applying a reference voltage source \bar{V} at the integrator input for a precisely known time interval Δt , then comparing the measured flux $\Delta\Phi$ to the

expected result:

$$k_{\text{int}} = 1 - \frac{\Delta\Phi}{\bar{V}\Delta t} \quad (2.15)$$

The uncertainties of both reference voltage and integration time are as low as a few ppm and can be neglected. The major remaining source of uncertainty is the repeatability of the flux measurement, which is affected by integrator drift and is typically about 50 ppm.

2.3.4 Reference-to-ring error, α

The magnets of a series production will often differ slightly due to assembly tolerances, or possibly errors in the number of yoke laminations (even if these are usually shuffled to minimize the impact of material property variations). In the case of ELENA, for contingent reasons, the yoke of the reference magnet was made of a different type of steel than the other seven magnets (the six in the ring, plus a spare), making them substantially different. Introducing an appropriate scaling factor is thus especially important in this case. To define it, we must consider that presently operational magnetic cycles are optimized at a lower maximum current level than the cycles used during the acceptance tests, which were intended to cover the full design range. The following magnetic measurement campaigns were carried out:

- acceptance cycles up to 326 A @ 200 A/s: all magnets;
- operational cycles up to 276 A @ 115 A/s: reference and spare magnet only.

The relationship between magnets is best expressed as a function of the current in terms of the so-called integral transfer function (shown in Fig. 2.3a):

$$\mathcal{T}(I; \dot{I}) = \frac{\mathbb{I}(t(I))}{I} \quad (2.16)$$

that is, for a cycle with a given nominal \dot{I} , the ratio between field and excitation current. (note that this expression and the following ones have two values, one for each branch of the hysteresis loop). The measurements show a good linearity on the up-ramp but a width of the hysteresis loop of about 2%, very large when compared to other accelerators (e.g. 0.5% in the PS Booster). This is especially relevant since ELENA is the only machine expected to accelerate and decelerate particles on the same cycle (as needed for commissioning of the electron cooler. Parameterization in terms of \dot{I} is needed to account for the impact of eddy current losses on the width of the hysteresis loop, as well visible in Fig. 2.3b. The scaling factor can then be defined as a function of the excitation current I :

$$1 + \alpha(I; \dot{I}) = \frac{\mathcal{T}_{\text{ring}}(I; \dot{I})}{\mathcal{T}_{\text{ref}}(I; \dot{I})} \quad (2.17)$$

where the subscripts ref and ring denote respectively the reference magnet and the average of the magnets in the ring. Assuming that the impact of a ramp rate change is approximately the same for

all magnets, an intermediate scaling factor between 200 and 115 A/s has been derived from results on the spare unit only (see Fig. 2.3b):

$$\chi(I; 115) = \frac{\mathcal{T}_{\text{spare}}(I; 115)}{\mathcal{T}_{\text{spare}}(I; 200)} \quad (2.18)$$

Operation cycles include some plateaus, during which the field varies while the current is constant and eddy currents decay; therefore, the curves have been smoothed to avoid discontinuities. The result can be used to extrapolate acceptance test results to the operational conditions according to (see the example for ramp-down in Fig. 2.3c):

$$\mathcal{T}_{\text{ring}}(I, 115) = \chi(I, 115) \mathcal{T}_{\text{ring}}(I, 200) \quad (2.19)$$

$$\mathcal{T}_{\text{ref}}(I, 115) = \chi(I, 115) \mathcal{T}_{\text{ref}}(I, 200) \quad (2.20)$$

Finally, the scaling factor between reference and ring in the operational conditions, shown in Fig. 2.3d, can be expressed as:

$$1 + \alpha(I, 115) = \frac{\mathcal{T}_{\text{ring}}(I, 200)}{\mathcal{T}_{\text{ref}}(I, 115)} \frac{\mathcal{T}_{\text{spare}}(I; 115)}{\mathcal{T}_{\text{spare}}(I; 200)} \quad (2.21)$$

The computed scaling factor is reasonably stable on the down-ramp of the antiproton decelerating cycle, which is the most important operational condition. Since, at the moment, the hardware does not implement variable coefficients in real-time, an average value is being used for operation, while the standard deviation of the residual is taken as an estimate of the associated uncertainty:

$$\bar{\alpha} = \frac{1}{I_{\text{max}} - I_{\text{min}}} \int_{I_{\text{min}}}^{I_{\text{max}}} \alpha(I, 115) dI \approx 0.999 \quad (2.22)$$

$$u(\alpha)^2 = \frac{1}{I_{\text{max}} - I_{\text{min}}} \int_{I_{\text{min}}}^{I_{\text{max}}} (\alpha(I, 115) - \bar{\alpha})^2 dI \quad (2.23)$$

$$\Rightarrow u(\alpha) \approx 3.2 \times 10^{-4}$$

On the other hand, the variation of the scaling factor on the up-ramp of the accelerating cycle appears to be much larger, about 0.5%, leading to a larger uncertainty $u(\alpha) \approx 1.45 \times 10^{-3}$. This might be attributed to different level of remanent field in the reference and ring magnets, since this quantity has an impact on the up-branch of the hysteresis loop of the transfer function, as this approaches the mid-range linear region.

2.3.5 Coil offset factor, ε

The factor ε accounts for the difference Δx between the transversal position of the induction coil and the nominal beam path, as shown in Fig. 1.6. The coil of the operational system lies approximately on the magnet's axis, while for the spare system $\Delta x = 22$ mm. The major contribution to the non-uniformity is given by the in-built integrated field gradient:

$$\mathcal{G}(t) = \int_{-\infty}^{+\infty} \frac{dB(t,s)}{dx} ds \approx 0.208 \text{ Tm/m} \quad (2.24)$$

This is due to the sector shape of the poles, and plays an important role in keeping the beam focused. The associated field error for the central coil, relative to the integrated field, can be expressed as:

$$\varepsilon(t) = \frac{\mathcal{G}(t)}{\mathbb{I}(t)} \Delta x \approx -6 \times 10^{-5} \quad (2.25)$$

for which the dependence upon the field level, hence the time, is well below 300 ppm and may thus be neglected. The uncertainty on ε is dominated by the uncertainty of the transversal offset, which was obtained by measuring the position of the induction coil relative to the magnet with a 3D laser tracker and can be quantified to about 0.2 mm.

2.3.6 Mapping the model to FPGA registers

As part of the B-train system, the FESA interface is used to set and get data from registers in the FPGA, which are used to calculate the magnetic field using the coil voltage and the NMR field markers. Equation 2.26 below shows the implemented calculation of the magnetic field in the FPGA, where *Flux* is the integral flux measured using the induction coil. The rest of the parameters are registers in the FPGA, which are set using the FESA interface.

Such a procedure is done since the implementation of the software was done before the measurement model was defined as in this document. Additionally, including a register for every parameter in the model would only increase the computational time of the measurement and transmission, which would be detrimental for real-time operation.

$$\bar{B}(t) = \text{Ponderation Factor} \left[\frac{\text{Correction Factor}}{\text{Coil width}} \cdot \text{Flux} + \text{Marker Level} \right] \quad (2.26)$$

Hence, combining Equations 2.10 and 2.26, it follows that:

$$\text{Ponderation factor} = \frac{1}{l^*} (1 + \alpha) (1 + \varepsilon) \quad (2.27)$$

$$\text{Coil width} = \bar{w}_{eff} \quad (2.28)$$

$$\text{Correction Factor} = (1 + \eta) \quad (2.29)$$

$$\text{Marker Level} = \mathbb{I}_0 \quad (2.30)$$

The full set of FESA setting values as of the end of 2018 is given in the Appendix.

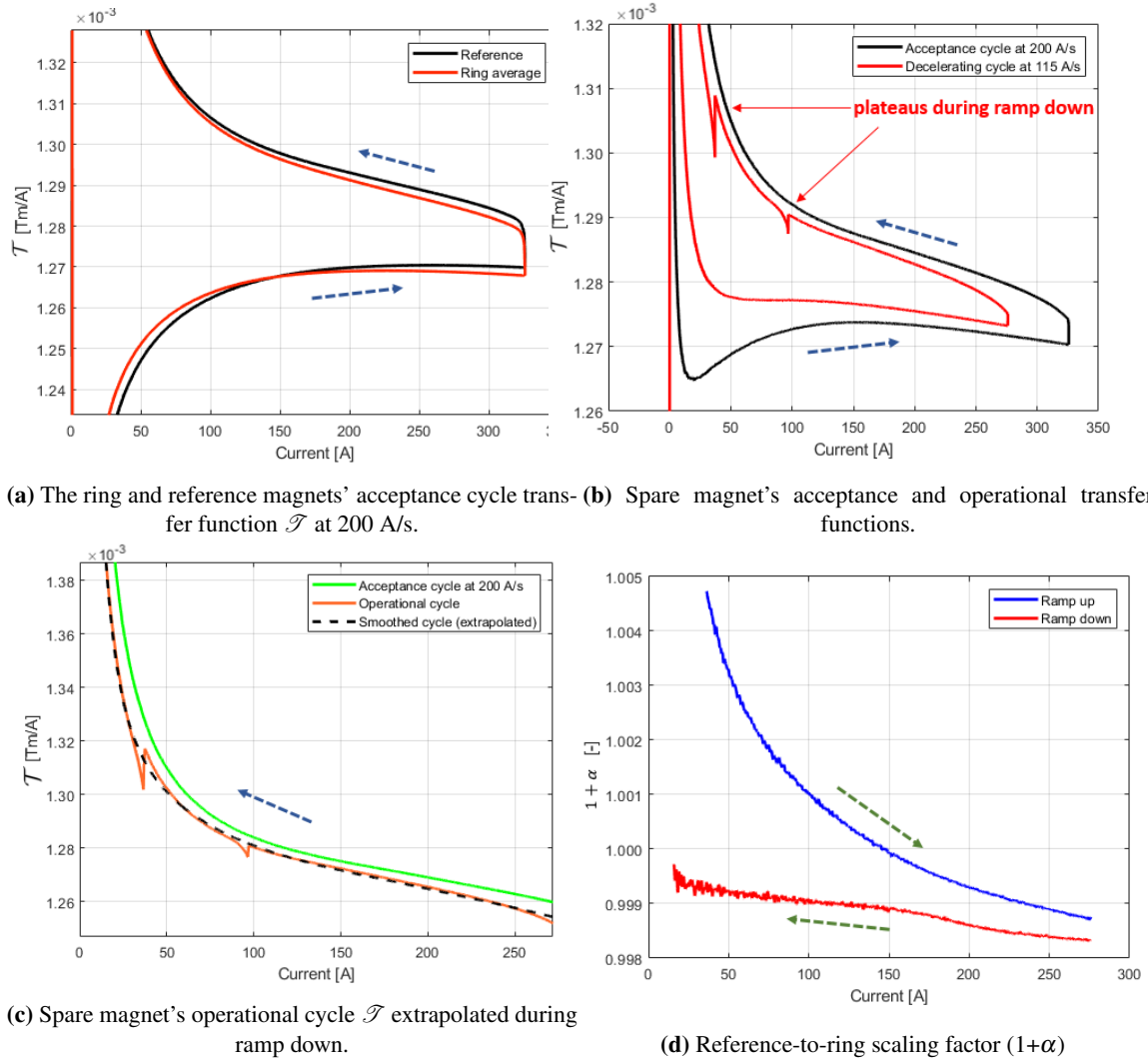


Fig. 2.3: Derivation of the reference-to-ring scaling factor. The ramp-up of the hysteresis cycles represents H^- ion acceleration, while the ramp-down represents antiproton deceleration



3 Uncertainty quantification

3.2 Introduction

This chapter aims to apply the linear forward uncertainty propagation method to the proposed measurement model. The goal of such a procedure is to quantify possible errors in measurements in operational circumstances before the system is operational. Knowledge of such errors can lead to better understanding of the system, and can allow planning for future optimizations of the software, which currently limits the implementation of the measurement model to its full potential.

3.3 Uncertainty quantification background

In every measurement system, its output is only an estimate of the quantity being measured. A quantitative evaluation of the measurement's uncertainty is necessary to give operators using the measurement system an idea of the errors involved in the measurement. It is also important in order to compare measurement results, either between themselves or with standard reference values. The 'Guide to the expression of uncertainty in measurement' (GUM) [16] separates the uncertainties in the result of a measurement into two main categories:

- Type A: uncertainties evaluated through repeated observations of the component.
- Type B: uncertainties evaluated by means other than statistical analysis of series of observations, generally using available knowledge.

The purpose of such a classification is to show that there are two different ways of classifying uncertainties. There is no difference in the nature of these elements resulting from these two types of evaluations. Uncertainty components from both types are quantified by variances or standard deviations. The proposed method for uncertainty quantification in the B-train system is to perform an uncertainty estimation to derive the combined standard uncertainty and to perform an uncertainty source classification to determine the effect and related significance of each uncertainty source.

The standard approach for uncertainty quantification uses the linear uncertainty propagation method, which is the first-order Taylor series approximation of the variance. This method applies only for linear models. In the case of non-linear models, the Supplement 1 to the GUM [17] recommends a Monte Carlo approach. This method however, requires significant computational time, as the accuracy of this method depends on the amount of runs and also fails to identify the contribution of each quantity's uncertainty to the combined standard uncertainty [18]. Unlike the Monte Carlo approach, the linear uncertainty propagation method does not underestimate a linear model's uncertainty when the experimental standard deviation of each quantity is known. Other approaches

for non-linear models are the Unscented Transform, which was applied for magnetic field measurements using rotating coils [19] and fuzzy variables [20].

3.3.1 Determining the combined standard uncertainty

The proposed method is the linear uncertainty propagation method. In general, in a measurement system, the measurand Y is not measured directly but derived using N quantities X_1, X_2, \dots, X_N through the function f :

$$Y = f(X_1, X_2, \dots, X_N) \quad (3.1)$$

The set of quantities X_1, X_2, \dots, X_N include values and uncertainties obtained from real-time and previous measurements as well as other quantities which are calibrated measurement standards such as mathematical constants.

An estimate of the measurand y , using input estimates x_1, x_2, \dots, x_N is given by:

$$y = f(x_1, x_2, \dots, x_N) \quad (3.2)$$

The estimated standard deviation associated with measurement output y , combined standard uncertainty $u_c(y)$, is derived from the estimated standard deviation of each input estimate x_i , termed standard uncertainty $u(x_i)$. In the determination of the combined uncertainty, all quantities will be assumed to be independent. This is based on the notion that all quantities have been measured repeatedly but not simultaneously in different independent experiments. GUM [16] defines $u_c(y)$ as the positive square root of the combined variance $u_c^2(y)$, given by:

$$u_c^2(y) = \sum_{i=1}^N \left(\frac{\delta f}{\delta x_i} \right)^2 u^2(x_i) \quad (3.3)$$

where $f(x_i)$ is the measurement model, and each $u(x_i)$ is obtained from characterization/calibration measurements.

3.4 Combined uncertainty of the ELENA B-train system

The measurement model used in the ELENA B-train can be summarised as in Equation 3.4, where $\Delta\Phi(t)$ represents the change in flux measured by the fluxmeter coil:

$$\bar{B}(t) = \frac{1}{l^*} (1 + \alpha) \cdot (1 + \varepsilon) \left[\frac{1 + \eta}{\bar{w}_{eff}} \Delta\Phi(t) + B_{NMR_n} \cdot l_m \right] \quad (3.4)$$

The uncertainty function can be defined as below, where the factors included are those which present uncertainty in the model, due to the method used to acquire them.

$$\bar{B}(t) = f((1 + \alpha), (1 + \varepsilon), (1 + \eta), \bar{w}_{eff}, \Delta\Phi(t), l_m) \quad (3.5)$$

Table 3.1: Uncertainty components of the ELENA measurement model at injection level

Parameter, p_i	Value	$u(p_i)$	$\left(\frac{\partial \bar{B}}{\partial p_i}\right) u(p_i) [\mu\text{T}]$	Source of uncertainty
α	0.0012	3×10^{-4}	221	Assumption that this factor is a constant (Type B)
ε	-6×10^{-5}	1.05×10^{-4}	73	Uncertainty on the transversal coil position measurement (Type A)
\mathbb{I}_0	326.836 mTm	13 μTm	13	Repeatability of high field marker integration constant (Type A)
\bar{w}_{eff}	2.84146 m	80 μm	10	Repeatability of the coil width calibration (Type A)
$\Phi(t)$	0.99411 Tm ²	30 μTm^2	10	Repeatability of flux measurement (Type A)
η	0.002475	7×10^{-6}	3	Effect of temperature fluctuations on coil resistance (Type A)

Applying the law of forward propagation, the partial derivative of the function with respect to each parameter has to be obtained. It has to be noted that the flux is considered to be a variable, and only the high-field NMR marker is considered in this case, as it is applied at all times and it corrects any fluctuations in the low-field marker itself.

$$\frac{\partial \bar{B}}{\partial \alpha} = \frac{(1 + \alpha)}{l^*} \left[(1 + \eta) \frac{\Delta \Phi(t)}{\bar{w}_{\text{eff}}} + \mathbb{I}_0 \right] \quad (3.6)$$

$$\frac{\partial \bar{B}}{\partial \varepsilon} = \frac{(1 + \alpha)[(1 + \eta)\Delta \Phi(t) + \mathbb{I}_0 \bar{w}_{\text{eff}}]}{l^* \bar{w}_{\text{eff}}} \quad (3.7)$$

$$\frac{\partial \bar{B}}{\partial \eta} = \frac{(1 + \alpha)(1 + \varepsilon)\Delta \Phi(t)}{l^* \bar{w}_{\text{eff}}} \quad (3.8)$$

$$\frac{\partial \bar{B}}{\partial \bar{w}_{\text{eff}}} = -\frac{(1 + \alpha)(1 + \varepsilon)(1 + \eta)\Delta \Phi(t)}{l^* \bar{w}_{\text{eff}}^2} \quad (3.9)$$

$$\frac{\partial \bar{B}}{\partial \Delta \Phi(t)} = \frac{(1 + \alpha)(1 + \varepsilon)(1 + \eta)}{l^* \bar{w}_{\text{eff}}} \quad (3.10)$$

$$\frac{\partial \bar{B}}{\partial \mathbb{I}_0} = \frac{(1 + \alpha)(1 + \varepsilon)}{l^*} \quad (3.11)$$

Table 3.1 summarizes the contribution of each uncertainty component for the deceleration cycle at the injection level where a flux change of 0.9944 Vs is measured by the fluxmeter.

According to [16], we then derive the combined standard uncertainty of the average field measurement $u_c(\bar{B})$ as:

$$u_c(\bar{B}) = \sqrt{\sum_{i=1}^N \left(\frac{\partial \bar{B}}{\partial p_i} \right)^2 u^2(p_i)} \quad (3.12)$$



where we shall assume that all variables are normally distributed and independent from each other. We remark that α , \bar{w}_{eff} and ε represent a systematic influence on the measurement, rather than a random effect like integrator drift. Table 3.1 shows the individual standard deviation of each parameter for the ELENA measurement system at injection level, when a decelerating cycle is applied. The resulting combined uncertainty at injection is:

- Ramp-down: $u_c(\bar{B}) = 2.3 \times 10^{-4}$ T (640 ppm)
- Ramp-up: $u_c(\bar{B}) = 5.6 \times 10^{-4}$ T (1560 ppm)

These figures, which are dominated by the error inherent in the extrapolation from the reference magnet to the average of the ring, represent the uncertainty at beam injection; in fact, the uncertainty varies as a function of time, although this aspect goes beyond the scope of this paper.

3.5 Conclusion

The measurement uncertainty is dominated by the errors inherent in the extrapolation to the ring and the position of the coil. As discussed above, both these factors are highly specific to ELENA, so substantially better performance can be expected for the other similar systems currently under commissioning. The impact of the uncertainty of α can be mitigated by selecting a different optimal value, typically corresponding to the critical time of particle injection, for each different magnetic cycle. A new software facility to update automatically the parameters in real-time has been implemented and is currently being tested, as part of the ongoing commissioning of the machine in a wide variety of operational configurations.



4 Metrological Characterization and Verification

4.1 Introduction

The metrological performance of a B-train system in real time can be evaluated through three categories of properties: various quality indicators which measure the quality of the output signals, statistical magnetic measurement indicators which indicate the repeatability/reproducibility of the output signal over several cycles, as well as beam-related quality indicators where a field measurement error would lead to instabilities in the beam performance.

4.2 Characterizing ELENA B-train performance

4.2.1 Error characterization model

The metrological capability of a measuring instrument can be determined by characterizing the two components of measurement error, the first one, random error, causing inconsistencies in the repeatability of the measurement in the form of scatter, whilst the second component, systematic error, causes a consistent difference between the measured and reference quantity values [21]. Considering the above definitions, the simplest model for defining the errors in B-trains is a linear, additive error model [22]:

$$\bar{B}(t) = (1 + \lambda)\bar{B}_0(t) + \Delta B + \varepsilon(t) \quad (4.1)$$

where $\bar{B}(t)$ refers to the measured and transmitted B-train output whilst $\bar{B}_0(t)$ refers to the actual magnetic field value. The three terms on the right-hand side represent three separate sources of errors. The first term, with an error parameter $(1 + \lambda)$, represents a scale error, when λ deviates from zero. The second term, ΔB , represents a bias, and can be called the offset error. These two terms jointly quantify the systematic error. The third term, ε indicates the random error, typically assumed as independent and identically distributed.

4.2.2 Definitions

The quality of each signal produced by the B-train sensors can be defined by several quantities explained below. Such quantities associated with a chain can be evaluated independently during those stretches of signal where the field is expected *a priori* to be stable, i.e. when the excitation current is stable and sufficient time has elapsed from the end of a previous ramp for eddy currents to decay.

Systematic errors can be evaluated by comparing directly the measured FIRESTORM chains among themselves, and finding the gain and offset differences, at a time instant t .

Drift is the most significant error when integrating the coil voltage. A small offset voltage is caused by the parasitic currents in the electronics and thermoelectric effects, leading to a drifting output when integrated. This error is reduced by the B-train at frequent intervals where the current is known to be constant. The average drift rate, $\langle \dot{B}(t) \rangle$, in T/s can be evaluated as shown in Equation 4.2, when the current is constant and there are no transient effects. An appropriate correction has to be made for the excitation current drift whenever it is known.

$$\langle \dot{B}(t) \rangle = \frac{\bar{B}(t + \Delta t) - \bar{B}(t)}{\Delta t} - \frac{d\bar{B}}{dI} \langle \dot{I}(t) \rangle \quad (4.2)$$

The drift in the measurement is normally observed within a cycle period, as it is expected that the use of a field marker reduces the cycle-to-cycle drift to zero, when a correction is applied to the cycle at t_k . In determining the drift, a linear curve is fitted to the B-train output signal at the end of a plateau, due to the lack of transient effects at that point. It is worth noting that tuning the drift in the ELENA B-train is more critical than in the other three systems as the cycles are much longer, and hence the drift has more influence on the measured field.

The random noise measured with respect to the average represents the lowest-level error i.e. the measurement resolution. The standard deviation of the $\bar{B}(t)$ points over a specific time period starting from t_0 gives a complete description. Otherwise, the peak-to-peak value gives a better estimate of the maximum error to be expected. The value of the noise contribution, σ_n , can be obtained according to (4.3), which is a measurement evaluated over a plateau with no transient effects present:

$$\sigma_n = \sigma(\bar{B}(t_0 + t_n) - \bar{B}(t_0) - \langle \dot{B}(t) \rangle (t_n)) \quad (4.3)$$

Another random error source, the field marker contribution, is the error introduced by the different trigger generation time of the field marker sensor. This error source can be evaluated by the repeatability of the sensor, carried out by calculating the standard deviation of the trigger time, $\sigma(t_k)$, over several cycles. Converting this jitter in seconds to an equivalent magnetic field value, the marker's error contribution is calculated by multiplying $\sigma(t_k)$ with the ramp rate at the trigger time $\dot{B}(t_k)$:

$$\sigma_m = \dot{B}(t_k) \sigma(t_k) \quad (4.4)$$

The marker time jitter gives a measure of the repeatability of the marker itself; however, such an indicator is also affected by the fluctuations in the current signal. Hence, we expect that:

$$\sigma_m \gtrsim \frac{d\bar{B}}{dI} \sigma(I_k) \quad (4.5)$$

where I_k represent current upon reception of the marker trigger. In operation, a higher apparent jitter will be observed due to unavoidable current fluctuations as a function of time; this is to be considered as an upper bound of the actual error.



4.2.3 Results

Tables 4.1 show the measurements recorded for two types of cycles: acceleration and deceleration cycles respectively. The quality measurements were recorded during repetitions of the cycles for both the operational system (C1) as well as the spare system (C2). Due to effects which are very difficult to measure, some measurements are not included for all types of cycles.

Table 4.1: ELENA B-train quality indicators

Parameter	Unit	Acceleration		Deceleration	
		C1	C2	C1	C2
Correlation of chains (Gain)	-	0.9992			
Correlation of chains (Offset)	G	2.084			
Average drift rate, $\langle \dot{B}(t) \rangle$	G/s	0.010 ± 0.015	-0.063 ± 0.021	0.010 ± 0.015	-0.063 ± 0.021
Average drift at injection $\langle \dot{B}(t) \rangle (t_{inj} - t_k)$	G	0.0049 ± 0.0074	-0.031 ± 0.010	0.0041 ± 0.0062	-0.026 ± 0.0087
Average drift at extraction $\langle \dot{B}(t) \rangle (t_{ex} - t_k)$	G	0.0069 ± 0.010	-0.044 ± 0.015	0.28 ± 0.42	-1.74 ± 0.058
Measured St. dev. noise level	G	0.029 ± 0.001			
Measured peak-to-peak noise level	G	0.138 ± 0.005			
Marker signal amplitude	V	0.16 ± 0.02	0.94 ± 0.05	0.18 ± 0.02	1.03 ± 0.05
				1.7 ± 0.03	1.7 ± 0.03

Table 4.2: ELENA B-train stability indicators

Parameter	Unit	Acceleration		Deceleration	
		C1	C2	C1	C2
Measured field repeatability @ injection $\sigma(t_{inj})$	G	0.039	0.043	0.041	0.043
Measured field repeatability @ extraction, $\sigma(t_{ex})$	G	0.041	0.044	0.37	0.54
Marker jitter repeatability, $\sigma(t_k)$	μs	60.1	9.7	69.6	10.3
Marker relative repeatability $\dot{B}(t_k)\sigma(t_k)/B(t_k)$	$\times 10^{-4}$	1.3	0.19	1.5	0.2
				0.10	0.16

4.3 Metrological verification with beam

In synchrotrons with no historic calibrated B-train, the actual magnetic field is not readily available, however by evaluating radio-frequency parameters, one can derive the magnetic field error as a function of time. The radio-frequency in a circular synchrotron varies during the acceleration ramp to keep the particles on a centred orbit. In order for the particle to stay exactly on the centred orbit, the radial component of the magnetic force must compensate the charge of the particle. The value of the programmed revolution frequency of the beam by the Low-Level RF system (LLRF) [23] is

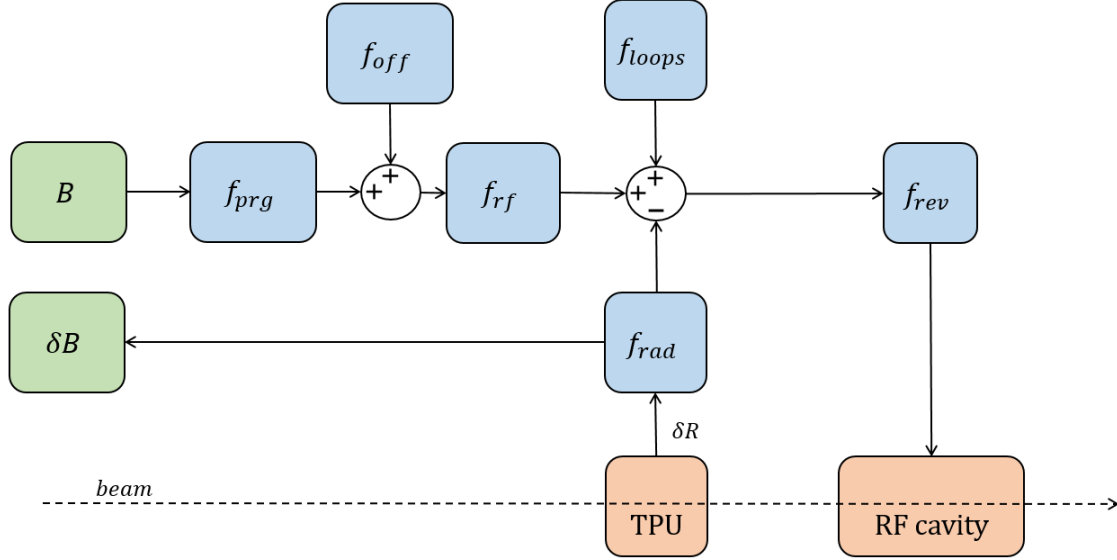


Fig. 4.1: Simplified schematic diagram of the LLRF system

determined according to Equation 4.6, with the value of $\bar{B}(t)$ transmitted from the B-train:

$$f_{prg}(t) = \frac{c}{2\pi R} \cdot \sqrt{1 - \frac{1}{1 + \left(\frac{\bar{B}(t)\rho q}{m_0 c}\right)^2}} \quad (4.6)$$

where c is the speed of light in vacuum, R is the mean orbit radius, q is the particle's charge and m_0 is the particle's rest mass.

An absolute error by the B-train can be compensated by the LLRF system through a frequency offset f_{off} , which is applied to the frequency $f_{rf}(t)$, as can be seen in Equation 4.7.

$$f_{rf}(t) = f_{prg}(t) + f_{off} \quad (4.7)$$

The revolution frequency applied to the cavity, $f_{rev}(t)$, is based on the frequency contribution of several feedback loops, as can be seen in Equation 4.8, where $f_{rad}(t)$ represents the radial loop frequency contribution, whilst, for the purpose of this study, the contributions of the phase loop, injection and extraction synchro loops are bundled up as one component, $f_{loops}(t)$.

$$f_{rev}(t) = f_{rf}(t) - f_{rad}(t) + f_{loops}(t) \quad (4.8)$$

In this study, we are only concerned with the radial loop frequency contribution, as this is the frequency component compensating for the beam radial position error, δR , based on several transverse pick-up units (TPU) placed along the ring [24]. The measured B-train calibration error, $\delta B(t)$

is hence obtained using the inverse of Eq. 4.6, by finding the field error based on $f_{rad}(t)$. Fig. 4.1 summarizes the LLRF's operation in a simplified manner with particular emphasis on the radial feedback loop. The beam position and bunched intensity are measured when the LLRF system is on, and hence when the beam is bunched. In the case of the ELENA, the TPU intensity measurement was acquired as an indicator of the presence of a bunched beam.

In the case of a new system such as in the ELENA, knowledge of the field error can be used to verify the B-train's setup and parameter identification methods and compensate for any systematic offsets caused by integrator gain errors or sensor characterization errors. The metrological verification is carried out by measuring the error $\delta B(t)$ along the cycle where the LLRF system is on. Redefining Eq. 4.1 to represent the error $\delta B(t)$ with respect to the measured $\bar{B}(t)$:

$$\delta B(t) = \bar{B}(t) - \bar{B}_0(t) \quad (4.9)$$

Substituting Eq. 4.9 in Eq. 4.1:

$$\delta B(t) = \lambda \bar{B}_0(t) + \Delta B + \varepsilon(t) \quad (4.10)$$

4.3.1 Experimental results

By fitting the measured $\delta B(t)$ values at different time-stamps over repeated cycles, the values of λ and ΔB can be obtained and compensated for. Before this procedure was applied to the ELENA B-train, all the parameters were setup according to the measurement model described in [25], resulting in an uncertainty of 0.23 mT at injection. Following the availability of the beam in the synchrotron, the calibration could be performed by measuring the radial loop frequency and its equivalent magnetic field value.

As can be seen in Fig. 4.2, measurements were taken repeatedly at several points where the beam is bunched. Fig. 4.3 shows the $\delta B(t)$ over the range of measurements acquired, before and after the calibration procedure. A line of best fit was calculated over the former set of measurements, resulting in a fit with $\lambda = -0.0026$ and $\Delta B = 0.77$ mT. This results in an absolute error of 0.16 mT at injection before calibration, well within the uncertainty estimation.

Nevertheless, the calibration was carried out by removing the systematic bias and another measurement campaign was held to characterize the system, which in the end was found to exhibit a scale error $\lambda = 6.3 \times 10^{-6}$ and an offset $\Delta B = -1.3 \mu\text{T}$ over the operational range of the LLRF system during deceleration. This is acceptable due to the fact that for the whole range $B(t)$ values, the systematic error is within the random error range. A final observation was made by turning the radial loop off, which meant that no feedback mechanism was in place, and as a result, the beam was still injected in the ring and extracted. On the other hand, in the PSB B-train, using the legacy B-train output as $\bar{B}_0(t)$, the consolidated B-train output is correlated with $\lambda = 50 \times 10^{-6}$ and $\Delta B = -14 \mu\text{T}$.

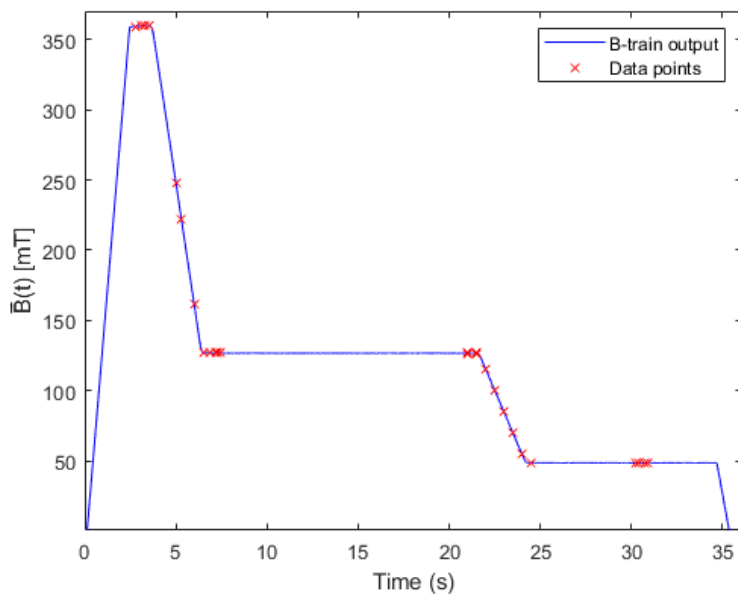


Fig. 4.2: The different points in the ELENA cycle where data was acquired repeatedly

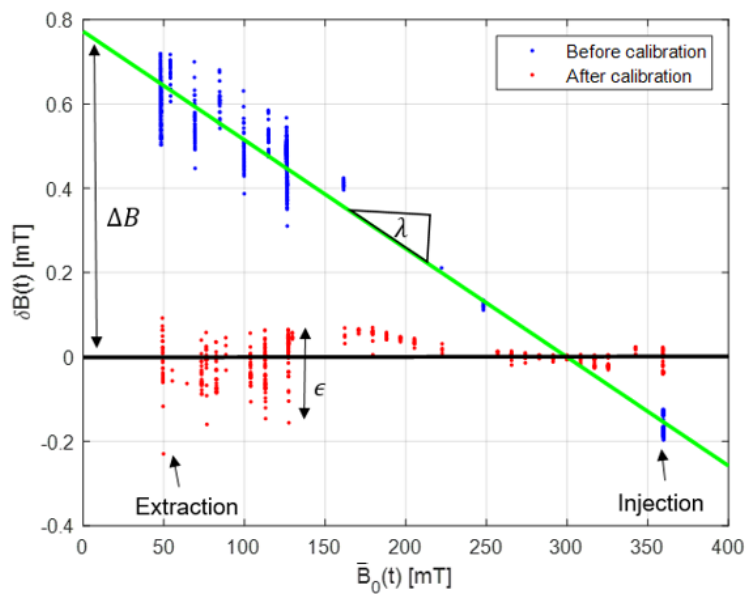


Fig. 4.3: $\bar{B}_0(t)$ vs. $\delta B(t)$ before and after the ELENA B-train's calibration



Table 4.3: ELENA B-train stability indicators

Parameter	Unit	Deceleration
Revolution frequency @ inj., $f_{rev}(t_{inj})$	kHz	1043.4 ± 0.063
Revolution frequency @ intermed., $f_{rev}(t_{int})$	kHz	371.2 ± 0.008
Revolution frequency @ ext., $f_{rev}(t_{ex})$	kHz	144.0 ± 0.107
Mean radial position @ inj., $\bar{r}(t_{inj})$	mm	-0.353 ± 0.008
Mean radial position @ intermed., $\bar{r}(t_{int})$	mm	-0.430 ± 0.017
Mean radial position @ ext., $\bar{r}(t_{ex})$	mm	1.596 ± 0.110
Mean radial loop frequency @ inj., $f_{rad}(t_{inj})$	Hz	34.4 ± 55
Mean radial loop frequency @ intermed., $f_{rad}(t_{int})$	Hz	-95 ± 48
Mean radial loop frequency @ ext., $f_{rad}(t_{ex})$	Hz	116 ± 153
Scaling error, λ	$\times 10^{-6}$	6.3
Offset error, ΔB	G	-0.013
Systematic error @ inj., $\lambda \bar{B}(t_{inj}) + \Delta B$	G	0.0097
Systematic error @ ext., $\lambda \bar{B}(t_{ex}) + \Delta B$	G	-0.0099



Conclusions

We formulated a measurement model which can predict the average bending magnetic field of a synchrotron, based on real-time magnetic field measurements from sensors located within a distinct reference magnet. This model is currently implemented in a simplified form in the ELENA decelerator ring at CERN, where all parameters have been assigned suitably averaged constant values as listed in Table 3.1. So far, the accuracy of the measurement has proven adequate for operation of the machine during the commissioning phase, with no need for additional empirical adjustment. This successful result is a first in the decade-spanning history of these systems at CERN. Providing an absolute value of the field, qualified with a formally derived uncertainty, represents an important shift of perspective as it gives operators a clear hint whether to investigate first the magnetic field, or other subsystems, whenever beam instabilities or other issues arise. In addition, we have developed a calibration procedure for the integration constant \mathbb{I}_0 that allows to use reliably an induction coil to obtain precise absolute measurements, and that can be effectively repeated *in-situ* to adapt to new accelerator cycles.

As a logical future extension, the possibility of implementing dynamically the scaling factor $1+\alpha$ in the real-time post-processing FPGA firmware is being considered as a way to reduce considerably this error source, bringing $u(\alpha)$ down to the level of the noise of the curves of Fig. 2.3d. We also plan to upgrade the FPGA hardware of the system to replace all constant parameters with functions of the excitation current or, equivalently, of the measured field. This will add the flexibility to adapt automatically the calibration constants such as \mathbb{I}_0 to any arbitrary cycle. Finally, the model will be expanded to include the effects of a constant background and time-varying stray fields from other magnets, which may affect the result to a level up to about 100 ppm.



Acknowledgements

The authors would like to thank the B-train colleagues Joseph Vella Wallbank, Vincenzo Di Capua and Maria Amodeo for useful discussion, exchange of information and support throughout the whole commissioning process. Thanks goes as well to Olaf Dunkel and Lucio Fiscarelli for their support on the calibration of the fluxmeter coil array and series measurements of the magnet.

In the case of measurements performed on the spare magnet, the authors would like to thank all TE-MSC-MM technical support personnel, especially Guy Deferne and Xavier Gontero for their help in setting up the spare magnet in the new magnetic measurements laboratory. A special thanks goes to Patrick Bestmann and Camille Vendeuvre from CERN's Alignment, Co-ordination and Engineering Group for their efforts and initiative when performing the laser tracker survey on the reference magnet.

The authors would also like to thank the whole ELENA operation crew led by Christian Carli and Tommy Eriksson, especially Lajos Bojtár, Bruno Dupuy, Pierre Freyermuth, Bertrand Lefort and Sergio Pasinelli for their patience when asking for specific magnetic cycles in the commissioning process.



Appendix - B-train FESA settings



09.11.2018 (Start of LS2)		Settings	FSBT_LNA_C1	FSBT_LNA_C2
1	Acquisitions	FEC	Btrain_DU.cfc-193-melenaop	Btrain_DU.cfc-193-melenaop
		Version	3.3.1	3.3.1
		DPotCH1	451	396
		DPotCH2	512	512
		GainMeasuredCH1	1.0000848	1.0003508
		GainMeasuredCH2	1.000108	1.0002398
		OffsetMeasuredCH1	7.63E-05	19.999847
		OffsetMeasuredCH2	6.87E-04	7.63E-05
2	Calculation factor	coil1_correctionFactor	1.00247	1.00247
		coil1_ponderationFactorB	1.0261	1.0261
		coil1_ponderationfactorBdot	0.005	0.005
		coil1_surface	2.8415	2.8601
3	Calibration Expert Settings	calibPotFactor	294444320	274444320
		timeDelayStartCalib	0.52	0.52
		voltageRef	8.75	8.75
4	CtimeDelay	delayAfterC0	0.175	0.175
5	DAC Selection	integrator1DACSelection	FocusB	FocusB
		integrator2DACSelection	FocusB	FocusB
		peak1DAC1Selection	CHAN1_ADC	CHAN1_ADC
		peak1DAC2Selection	CHAN2_DIFF	CHAN2_DIFF
		peak2DAC1Selection	CHAN1_DIFF	CHAN1_DIFF
		peak2DAC2Selection	CHAN1_DIFF	CHAN1_DIFF
6	DMA Expert Setting	decimationFactorB	2000	2000
		decimationFactorPeak	1000	1000
7	FMCExpertSetting	bmeas1_ch1	COIL_1	COIL_1
		mainIntegratorDevice	BMEAS1	BMEAS1
		peak1_ch1	NMR_M2	NMR_M2
		peak1_ch2	NMR_M1	NMR_M1
8	M1ExpertWindowSet	m1EnWin	TRUE	TRUE
		m1ForcedDelay	1	1
		m1PulseForced	FALSE	FALSE
		m1PulseWidth	0.1	0.1
		m1VThreshold	-0.9	-0.9
		m1WinDelay	480	480
		m1WinWidth	100	100
9	M2ExpertWindowSet	m1EnWin	TRUE	TRUE
		m1ForcedDelay	1	1
		m1PulseForced	FALSE	FALSE
		m1PulseWidth	0.1	0.1
		m1VThreshold	-2	-2
		m1WinDelay	1400	1400
		m1WinWidth	2100	2100



09.11.2018 (Start of LS2)	Settings	FSBT_LNA_C1	FSBT_LNA_C2
10 MarkerBLevel	m1MarkerAmplitude	0.8	0.8
	m1MarkerBLevel	0.043369	0.04336
	m1MarkerFrequency	0.001915924	0.001915924
	m1MarkerPower	3	3
	m2MarkerAmplitude	0.8	0.8
	m2MarkerBLevel	0.3276	0.32752
	m2MarkerFrequency	0.0024	0.0024
	m2MarkerPower	3	3
11 NMRMarkerExpertSetting	m1GpibAddress	5	5
	m1MarkerPosition	LOW	LOW
	m1MarkerProbe	1	1
	m1NMRName	NMR1	NMR1
	m1ProtConverterDHCPName	CBEGP-193-M-L1-C1	ELENA-MARKER1SP
	m1ProtConverterType	PROLOGIX	PROLOGIX
	m1SGAssociated	SG1	SG1
	m2GpibAddress	5	5
	m2MarkerPosition	HIGH	HIGH
	m2MarkerProbe	3	3
	m2NMRName	NMR2	NMR2
	m2ProtConverterDHCPName	HCCBEGC	HCCBEGC
	m2ProtConverterType	PROLOGIX	PROLOGIX
	m2SGAssociated	SG2	SG2
12 SGExpertSetting	m1SGOutputCmd	ON	ON
	m1SGState	Operation	Operation
	m1SGType	TG5011	TG5011
	m1SG_DHCP_Name	CFG-193-M-NMR-L-C1	CFG-193-M-NMR-L-C2
	m2SGOutputCmd	OFF	OFF
13 SoftMarker	c0IntReset	FALSE	FALSE
	extSoftMarker	ExternalMarker	ExternalMarker
14 TransferExpertSettings	ADC_CH1_sync	3	3
	ADC_CH2_sync	3	3
	dataTransferRate	250	250
	frameType	Bframe	Bframe
15 WriteRegister	addressRegister	0	0
	cardBus	IntegralCardBus	IntegralCardBus
	valRegister	0	0
	writeRegister	FALSE	FALSE
SIGNAL GENERATOR M2	Function=Square		
	Frequency=14.4758672 MHz		
	Amplitude=800 mVpp		
	Offset=0 V		
	DutyCycle=50%		
	Load impedance= high-Z		



Bibliography

- [1] CERN. Available: <https://cds.cern.ch/record/2235240>, 2016.
- [2] M. Benedikt, F. Caspers, and M. Lindroos, "Application of magnetic markers for precise measurement of magnetic fields in ramped accelerators," *Particle Accelerators*, no. 63, 1999.
- [3] L. Bottura and K. Henrichsen, "Field Measurements," *CERN Accelerator School - Superconductivity and Cryogenics for accelerators and detectors*, 2002.
- [4] C. Reymond, "Magnetic Resonance Techniques," in *CERN Accelerator School: Measurement and Alignment of Accelerator and Detector magnets* (S. Turner, ed.), pp. 219–232, CERN, 1998.
- [5] F. Caspers, "FerriMagnetic Resonance: A method to measure magnetic fields in accelerator environment," Tech. Rep. CERN-PS-AR-Note-94-21, CERN, 1994.
- [6] C. Grech, R. Avramidou, A. Beaumont, M. Buzio, N. Sammut, and J. Tinembart, "Metrological Characterization of Nuclear Magnetic Resonance Markers for Real-Time Field Control of the CERN ELENA Ring Dipoles," *IEEE Sensors Journal*, vol. 18, pp. 5826–5833, July 2018.
- [7] C. Grech, A. Beaumont, M. Buzio, and N. Sammut, "Performance Comparison of Nuclear Magnetic Resonance and FerriMagnetic Resonance field markers for the control of low-energy synchrotrons," in *IMEKO*, 2018.
- [8] T. Hoffmann, "FESA Primer," tech. rep., GSI, 2007.
- [9] W. Bartmann, P. Belochitskii, H. Breuker, F. Butin, C. Carli, T. Eriksson, S. Maury, S. Pasinelli, G. Tranquille, and W. Oelert, "Extra Low Energy Antiproton Ring ELENA: from the Conception to the Implementation Phase," *IPAC*, 2014.
- [10] G. Bertotti, *Hysteresis in Magnetism*. Academic Press, San Diego, 1998.
- [11] P. Dreesen and I. Garcia-Alfonso, "A new B-train system for the PS accelerator," tech. rep., CERN, 2002. <https://edms.cern.ch/document/2064859/1>.
- [12] C. Bovet, R. Gouiran, I. Gumowski, and K. H. Reich, *A selection of formulae and data useful for the design of A.G. synchrotrons*. Geneva: CERN, 1970.
- [13] M. Amodeo, "Metrological characterization of field markers for real-time measurement and control of accelerator magnets," Master's thesis, University of Naples Federico II, 2018.
- [14] M. Buzio, "Real Time Magnetic Field Control and Measurement." International Master in Hadrontherapy, Pavia, May 2013.



- [15] Agilent Technologies, *Agilent Technologies 34401A Digital Multimeter Manual*. Available: <http://literature.cdn.keysight.com/litweb/pdf/34401-90013.pdf>.
- [16] Joint Committee for Guides in Metrology, "Evaluation of measurement data: Guide to the expression of uncertainty in measurement," *International Organization for Standardization Geneva ISBN*, vol. 50, no. September, p. 134, 2008.
- [17] Joint Committee for Guides in Metrology, "Evaluation of measurement data: Supplement 1 to the Guide to the expression of uncertainty in measurement: Propagation of distributions using a Monte Carlo method," *International Organization for Standardization Geneva ISBN*, vol. JCGM 101:2, p. 90, 2008.
- [18] A. Badalyan, Z. You, K. Aji, P. Bedrikovetsky, T. Carageorgos, and A. Zeinijahromi, "Size exclusion deep bed filtration: Experimental and modelling uncertainties," *Review of Scientific Instruments*, vol. 85, no. 1, p. 015111, 2014.
- [19] P. Arpaia *et al.*, "Unscented transform-based uncertainty analysis of rotating coil transducers for field mapping," *Review of Scientific Instruments*, vol. 87, no. 3, p. 035004, 2016.
- [20] C. D. Capua and E. Romeo, "A t -norm-based fuzzy approach to the estimation of measurement uncertainty," *IEEE Transactions on Instrumentation and Measurement*, vol. 58, pp. 350–355, Feb 2009.
- [21] A. Giordani and L. Mari, "Modeling measurement: Error and uncertainty," in *Error and Uncertainty in Scientific Practice* (M. Boumans, G. Hon, and A. Petersen, eds.), pp. 79–96, Pickering & Chatto, 2014.
- [22] Y. Tian, G. S. Nearing, C. D. Peters-Lidard, K. W. Harrison, and L. Tang, "Performance Metrics, Error Modeling, and Uncertainty Quantification," *Monthly Weather Review*, vol. 144, no. 2, pp. 607–613, 2016.
- [23] M. E. Angoletta, S. Albright, S. Energico, S. Hancock, M. Jaussi, A. Jones, J. Molendijk, M. Paoluzzi, and J. Sanchez-Quesada, "Initial Beam Results of CERN ELENA's Digital Low-Level RF System," in *IPAC2017*, no. CERN-ACC-2017-264, (Copenhagen, Denmark), p. THPAB142. 4 p, May 2017.
- [24] R. Marco-Hernández, D. Alves, M. E. Angoletta, O. Marquersén, J. Molendijk, E. Oponowicz, R. Ruffieux, J. Sánchez-Quesada, and L. SØby, "The AD and ELENA orbit, trajectory and intensity measurement systems," *JINST*, vol. 12, no. 07, 2017.
- [25] C. Grech, M. Buzio, and N. Sammut, "A Magnetic Measurement Model for Real-Time Control of Synchrotrons," *IEEE Transactions on Instrumentation and Measurement*, Apr. 2019.